A Novel Short-Pathlength Photoreactor to Study Aqueous-phase Photochemistry: Application to Biomass-Burning Phenols

Christopher Niedek[1], Wenqing Jiang[1], Antai Zhang[1], Cort Anastasio[2], Qi Zhang[1*]

1 Department of Environmental Toxicology, University of California, 1 Shields Ave., Davis, California 95616, United States
2Department of Land, Air, and Water Resources, University of California, One Shields Avenue, Davis, California 95616-8627

* Correspondence to: Qi Zhang (dkwzhang@ucdavis.edu)

Abstract. Aqueous-phase oxidation of biomass-burning phenols is a significant but poorly constrained source of secondary organic aerosol (SOA) in the atmosphere. Laboratory studies replicating aerosol liquid water (ALW) – characterized by high solute and chromophore concentrations – remain scarce due to strong light attenuation and thermal gradients in conventional photoreactors. To address these limitations, we developed a short-pathlength photoreactor (SPP) that minimizes optical screening and provides precise control of temperature, humidity, and illumination conditions. Using guaiacyl acetone (GA) as a model phenol compound and 3,4-dimethoxybenzaldehyde (DMB) as a triplet precursor ($^3C^*$), the SPP successfully reproduced SOA yields from established photoreactors under dilute conditions and further enabled experiments under strongly light-absorbing ALW regimes. The system maintained stable temperature and relative humidity, consistent photon flux, and reproducible photochemical performance. Positive matrix factorization (PMF) of high-resolution aerosol mass spectra resolved distinct stages of GA-derived aqueous SOA (aqSOA) evolution across a wide range of ionic strengths. The analysis further revealed the formation of GA dimers through photosensitized coupling pathways, with dimer formation rates increasing significantly with ionic strength. Overall, the SPP provides a validated and versatile platform for investigating aqSOA formation and transformation processes under atmospherically relevant droplet and ALW conditions.

1 Introduction

Understanding secondary organic aerosols (SOA) formation in atmospheric aqueous phases is critical for improving predictions of regional air pollution and global climate change (Jimenez et al., 2009; Von Schneidemesser et al., 2015). While gas-phase oxidation of volatile organic compounds (VOCs) is well established as a major SOA source (Hodshire et al., 2019), aqueous-phase pathways in cloud, fog, and aerosol liquid water (ALW) remain comparatively underexplored (Ervens, 2015; Herrmann et al., 2015; Li et al., 2023; Tilgner et al., 2021). These condensed-phase processes generate highly oxidized, low-volatility organics that differ fundamentally from those formed via gas-phase pathways (Ervens, 2015; Jiang et al., 2024; McNeill, 2015; Zhang et al., 2024a). Neglecting such reactions contributes to persistent model-observation discrepancies in SOA mass and composition (Ervens et al., 2011; Shrivastava et al., 2017; Zhang et al., 2024b).

Biomass-burning (BB) is a major global source of oxygenated aromatics, notably phenols and furans, produced through pyrolysis of lignin and cellulose (Romanias et al., 2024; Schauer et al., 2001). Phenols, in particular, are highly reactive in aqueous environments and form aqueous SOA (aqSOA) with mass yields often exceeding 100% (Arciva et al., 2022; Huang et al., 2018; Jiang et al., 2021, 2024; Ma et al., 2021; Smith et al., 2014, 2015; Sun et al., 2010; Yu et al., 2014). Field and modeling studies further suggest that phenolic aqSOA contributes substantially to brown carbon and fine particulate matter ($PM_{2.5}$) in BB-impacted air masses (Farley et al., 2025; Gilardoni et al., 2016; Zhang et al., 2024b).

Most laboratory investigations of phenol photochemistry have focused on dilute aqueous systems representative of cloud and fog waters, characterized by high liquid water content (LWC; 0.05-1 g of water m^{-3} of air), low ionic strength (10^{-5}-10^{-2} M), and mildly acidic to near-neutral pH (Ervens et al., 2011; Herrmann et al., 2010, 2015; Pang et al., 2019; Tilgner et al., 2021). In contrast, ALW in fine particles can reach molar-level solute concentrations (Parworth et al., 2017), resulting in higher ionic strength (up to ~20 M) and effectively stronger light absorption by dissolved organics and nitrate. Such concentrated conditions significantly alter photochemical kinetics, phase partitioning, and product formation, yet remain challenging to represent in the laboratory. Specifically, high optical densities and thermal gradients in conventional centimeter-scale photoreactors limit light penetration and constrain experimental precision. For example, at ALW-relevant concentrations (e.g., 1 mM), 3,4-dimethoxybenzaldehyde (DMB) – a widely used photosensitizer in aqSOA studies – transmits less than 0.1% of UVA light (322 nm) across a 1-cm pathlength, compared with > 96% under cloud-water conditions (~ 5 μM). This disparity illustrates the severity of light-screening effects that arise under concentrated regimes. While ambient aqueous concentrations of phenols in ALW are poorly constrained, previous work suggests that salting-out may suppress phenol partitioning into the aqueous phase, while elevated dissolved organic matter (DOM) could increase it beyond predictions from Henry's Law (Capel et al., 1991; McFall et al., 2020; Sagebiel and Seiber, 1993). Depending on local emissions, inorganic species in ALW can range from micromolar to molar concentrations (Bianco et al., 2020; Parworth et al., 2017), significantly influencing the ionic strength and pH of the aerosol phase.

To date, only a limited number of lab studies have examined phenol photochemistry under ALW-like conditions. For instance, Ma et. al. (2021) studied the photosensitized degradation of guaiacyl acetone (GA) in 2 M salt solutions and observed only modest changes in phenol decay rates, while their modeling predicted non-linear aqSOA yields with varying particle-to-water mass ratio, highlighting the strong influence of LWC on phase partitioning and reactivity. Other studies have shown that ionic strength can substantially affect phenol solubility ((McFall et al., 2020; Mekic et al., 2020; Mekic and Gligorovski, 2021) and references therein), photodegradation kinetics (Zhou et al., 2019), and aqSOA chemical composition (Wang et al., 2021). Collectively, these results highlight the complex and system-dependent role of ionic strength in modulating aqueous photochemistry and SOA formation. However, accurately reproducing the optical and chemical environment of ALW in the laboratory, particularly the high ionic strength conditions, remains a significant experimental challenge.

To address these limitations, we developed a short-pathlength photoreactor (SPP) designed to investigate aqueous-phase photochemistry across both dilute and highly concentrated regimes. The SPP minimizes light attenuation and photothermal effects while allowing independent controls of temperature, relative humidity (RH), and optical pathlength. As a case study,

we investigated the photosensitized oxidation of GA by DMB, a model system previously characterized under cloud-relevant conditions (Jiang et al., 2021; Ma et al., 2021). Here, we evaluate the SPP's performance across a wide range of ionic strengths and UV absorption regimes, demonstrating its utility to reproduce and extend aqSOA experiments into the concentrated ALW conditions.

2 Materials and Methods

2.1 Chemicals

Guaiacyl acetone (GA; 96 % purity), 2-nitrobenzaldehyde (2-NB), ammonium sulfate (AS; ACS reagent grade), and isotopically enriched AS ($A^{34}S$; >98 % ^{34}S) were purchased from Millipore Sigma. Sodium sulfate (ACS grade), sodium borate (ACS grade), sulfuric acid (ACS Plus grade), and hydrogen peroxide (H_2O_2; 30 %, ACS grade) were obtained from Fisher Scientific. All solutions were prepared using ultrapure water (Milli-Q water; ≥ 18.2 MΩ cm).

To minimize organic contamination observed during preliminary tests at high sulfate concentrations, sodium sulfate was further purified. The purification involved preparing a 1000 mg L^{-1} sulfate solution in 50 mM H_2O_2 and irradiating it for 24 hours in quartz tubes using an RPR-200 photoreactor equipped with 254 nm lamps. The irradiated solution was then evaporated to dryness to remove residual H_2O_2 and re-dissolved in Milli-Q water to the desired concentration.

2.2 Photochemical experiments

This study employed three distinct photochemical systems: the short-pathlength photoreactor (SPP), the small tower (ST), and the RPR-200 photoreactor. The SPP features a modular design with an interchangeable light source. In this study, it was equipped with a 1000 W xenon arc lamp and downstream optical filters, including a water filter, AM1.0 air mass filter, 295 nm long-pass filter, and 400 nm short-pass filter, to approximate tropospheric sunlight (Hullar et al., 2020). The SPP employs a top-down illumination scheme which will be discussed further below. The system comprises a temperature-controlled base, an interchangeable reactor dish (100 mm diameter, 15 mm height), and a quartz window that seals the reactor dish while allowing for top illumination (Figure 1). The wide, shallow geometry, combined with top-down illumination, enables adjustable optical pathlengths by varying solution volume.

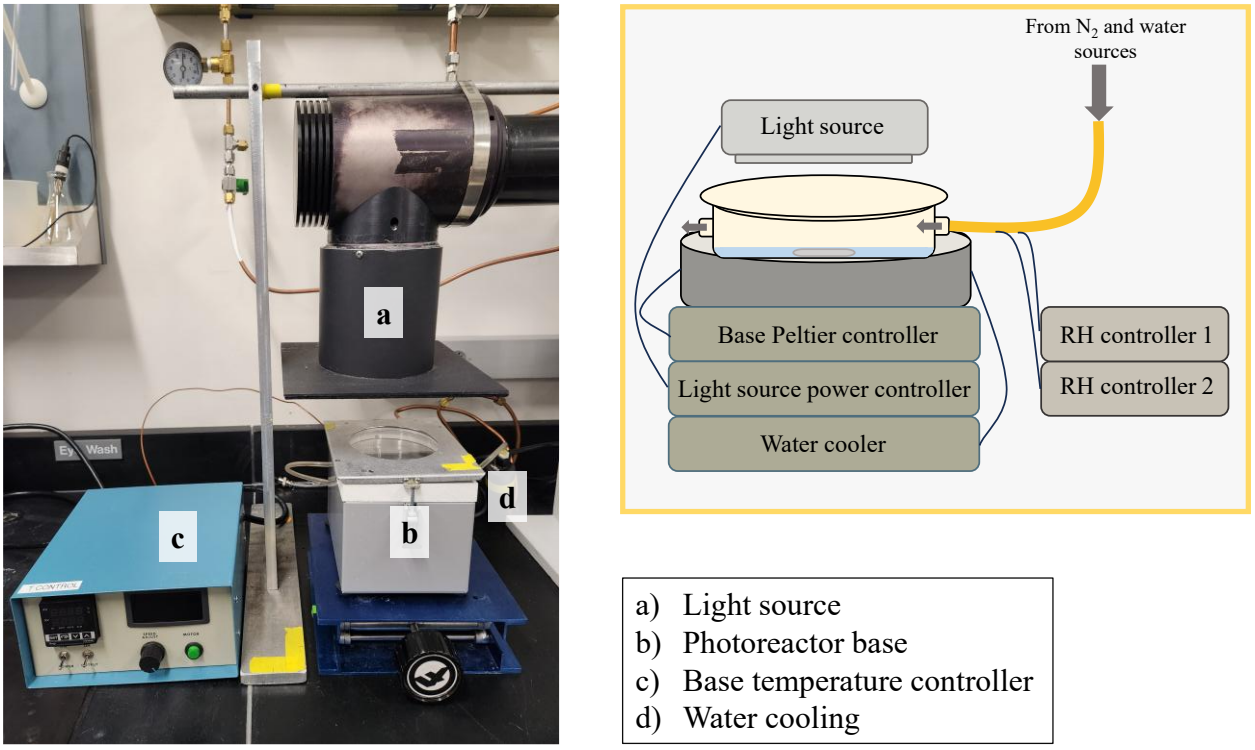

Figure 1: Photograph and schematic diagram of the photochemical experimental setup using the SPP. The photograph displays the setup used for all GA+DMB experiments while the diagram gives the generalized setup applicable to all experiments described in this study. A detailed description of the SPP system and operation is available in Section 0.

The ST system (Ma et al., 2021) uses the same xenon lamp and optical filters as the SPP, except for the 400 nm short-pass filter, and provides a spectral output that is nearly identical to the SPP in the 280-400 nm range. Samples are illuminated horizontally rather than from above using 2 cm cuvettes. The RPR-200 photoreactor employs three sets of fluorescent lamps centered at 300, 350, and 419 nm to crudely simulate solar radiation, generating triplet excited state carbon ($^3C^*$) levels ~7 times higher than typical wintertime ambient conditions (George et al., 2015; Jiang et al., 2021). The reaction vessels are 110 mL with 5 cm diameters. A comparison of the spectral characteristics of the three systems is provided in Figure S1. Photoreaction data collected using the SPP are compared with those from the ST and RPR-200 systems. Detailed descriptions of the RPR-200 and ST experimental setups can be found in Jiang et al. (2021) and Ma et al. 2021, respectively. The SPP was designed with the limitations of the ST and RPR-200 in mind, namely the long, rigidly defined optical pathlengths and large liquid volumes required.

Solution compositions for all experiments are summarized in Table 1. The RPR and ST systems used solution conditions representative of fog and cloud water, with sulfate introduced as either ammonium sulfate (AS), sodium sulfate (Na_2SO_4), or sulfuric acid (H_2SO_4). The SPP experiments examined a wider range of GA, 3,4-DMB, and sulfate concentrations. During illumination in both the SPP and ST systems, aliquots were periodically collected for chemical analysis. The RPR experiments

were performed using a combination of discrete aliquot collection for offline analysis and continuous solution withdrawal for real-time chemical measurements (Jiang et al., 2021). In the ST photoreactor, aliquots were taken at time points corresponding to 1, 2, and 3 half-lives ($t_{1/2}$) of GA decay (Ma et al., 2021). In the SPP, a total of 7-8 aliquots (300 μL each) were collected from the start of illumination through approximately $2\times t_{1/2}$. These samples were analyzed using high performance liquid chromatography (HPLC), UV-Vis spectroscopy, and high-resolution aerosol mass spectrometry. At the start of each experiment, the photon flux was quantified by measuring the photolysis rate constant (j_{2NB}) of a 10 μM 2-nitrobenzaldehyde (2-NB) solution, following the procedure of Galbavy et al. (2010).

Table 1: Summary of experimental parameters for each photoreaction. Experiments represented by a number were all performed using the SPP.

Exp. ID	Photoreactor	$[GA]_0$ (mM)	$[DMB]_0$ (mM)	$[SO_4]$ (mM)	$[GA]_0/[DMB]_0$	pH	$k'_{GA,WIN}$ (hr^{-1})[a]	$t_{1/2}$ (hr)[b]	SOA yield	Formation rates (mg L^{-1} $t_{1/2}^{-1}$)	
										$C_{18}H_{19}O_5^+$	$C_{14}H_{11}O_3^+$
Cloud/fog drop conditions											
RPR	RPR-200	0.1	0.005	0.104	20	4.6	1.3	0.53	0.83	N/A	N/A
ST	Small tower	0.1	0.005	0.0066	20	5	0.21	3.30	0.84	N/A	N/A
1	SPP	0.1	0.005	0.104	20	5	0.17±0.002	4.15	0.75	0.063	0.009
Constant $[GA]_0/[DMB]_0$ and $[SO_4]$, increasing $[GA]_0$											
2	SPP	0.5	0.025	0.104	20	4.8	0.33±0.008	2.27	0.72	0.29	0.063
3	SPP	1	0.05	0.104	20	5	0.24±0.008	4.11	0.56	0.41	0.13
4	SPP	1.5	0.075	0.104	20	4.8	0.29±0.004	3.28	0.44	1.4	0.18
5	SPP	2	0.1	0.104	20	4.8	0.38±0.02	2.88	0.76	3.7	0.62
Low $[GA]_0/[DMB]_0$ (<20), constant $[SO_4]$											
6	SPP	0.1	0.05	0.104	2	4.9	0.64±0.01	2.50	0.61	0.11	0.016
7	SPP	0.1	0.1	0.104	1	5.1	2.2±0.05	0.79	0.47	0.1	0.021
High $[GA]_0/[DMB]_0$ (>20), constant $[SO_4]$											
8	SPP	0.5	0.005	0.104	100	4.8	0.14±0.002	6.30	0.26	0.24	0.051
9	SPP	1	0.005	0.104	200	5	0.16±0.004	6.07	0.63	1.5	0.19
10	SPP	2	0.005	0.104	400	4.8	0.15±0.002	10.2	0.65	7	0.84
Constant $[GA]_0/[DMB]_0$, increasing $[SO_4]$											
11	SPP	2	0.1	10	20	4.9	0.26±0.003	4.14	0.83	5.5	0.95
12	SPP	2	0.1	100	20	5.1	0.26±0.005	3.74	N/A	6.7	0.88
13	SPP	2	0.1	1000	20	5.1	0.19±0.005	4.99	N/A	7.3	1.2

[a]Values for $k'_{GA,WIN}$ are the average ±1 standard error.

[b]$t_{1/2}$ is used for comparing formation rates across experiments.

2.3 SPP characterization experiments

For SPP characterization, individual salt samples were deliquesced and allowed to equilibrate to their water uptake masses under controlled RH and T conditions. Dry salts were placed in 0.5 ml clear polypropylene containers and introduced into the SPP reaction chamber after the targeted RH was reached and stabilized. Samples were periodically removed to record mass

changes and monitor water uptake as a function of time. Additionally, replicate photochemical experiments – performed using the procedure described in Section 2.2— were conducted to further evaluate the reproducibility and performance of the SPP under representative operating conditions.

2.4 Chemical analyses

GA decay was quantified using a Shimadzu HPLC system equipped with a photodiode array (PDA) detector. Samples were analyzed directly without additional processing. Separation was achieved on a ThermoScientific BetaBasic-18 C_{18} column (250 x 3 mm, 5 µm) with an isocratic mobile phase of 80:20 (v:v) water to acetonitrile, and GA and 3,4-DMB were detected at 280 nm.

The bulk chemical composition of collected aliquots was analyzed using a micronebulization-aerosol mass spectrometry (MN-AMS) system following Niedek et al. (2023). Briefly, each 200 µL aliquot was diluted with Milli-Q water, and isotopically enriched $(NH_4)_2{}^{34}SO_4$ was added as an internal standard to yield a final ${}^{34}SO_4{}^{2-}$ concentration of 10 mg L^{-1}. The diluted solution was delivered to a micronebulizer at 150 µL min^{-1} using a syringe pump, with heated (40 °C) high-purity N_2 serving as both carrier and atomization gas. The generated aerosol was dried using a diffusion drier and analyzed by an Aerodyne high-resolution time-of-flight aerosol mass spectrometer (HR-AMS; $m/\Delta m \approx 3000$) with 1-min signal averaging. The use of an AMS allows for direct measurements of the condensed-phase components of the phenolic SOA and for more direct comparisons to the broader literature of both real-time and offline measurements of SOA.

2.5 Data analysis

2.5.1 Kinetics calculations and corrections

Decay rates of GA and 3,4-DMB were determined from HPLC data. GA concentrations followed a first-order exponential decay, while 3,4-DMB followed a linear decrease (<20% loss for all experiments). Observed rate constants (k'_x) were normalized to the photolysis rate of 2-nitrobenzaldehyde ($j_{2NB,exp}$) measured in each experiment and scaled to a reference solar flux corresponding to the winter solstice at midday in Davis, CA ($j_{2NB,win}$ = 0.0070 s^{-1}; Anastasio and McGregor (2001)).

To correct for internal light attenuation, wavelength-dependent screening factors (S_λ) were calculated using the method from Smith et al. (2016):

$$S_\lambda = \frac{\sum[\left(1-10^{-\varepsilon_\lambda[C]l}\right)*I'_\lambda]}{\sum[(2.303*\varepsilon_\lambda[C]l)*I'_\lambda]} \quad (1)$$

where ε_λ is the molar absorption coefficient (M^{-1} cm^{-1}) at wavelength λ, [C] is the concentration of the absorbing compound (M), l is the optical pathlength (cm), and I'_λ is the wavelength-resolved photon flux (mol photons L^{-1} s^{-1} nm^{-1}). For multicomponent systems, total absorbance was summed before calculating S_λ. The corrected, normalized rate constant ($k'_{x,win}$) was then calculated as:

$$k'_{x,WIN} = \left[\frac{k'_x}{S_\lambda * j_{2NB,exp}}\right] * j_{2NB,WIN} \quad (2)$$

The chemical evolution of GA-derived aqSOA was characterized by tracking key tracer ions (e.g., $C_{14}H_{11}O_3^+$ and $C_{18}H_{19}O_5^+$ for GA dimers), with their time-dependent signals fit using a single exponential rise-to-plateau function:

$$y = y_O + A\,(1 - \exp(-k * t)) \quad (3)$$

where y_0 is the asymptotic value as t approaches infinity, A is an offset that sets y near 0 at $t = 0$, and k is the fitted rate constant, and t is expressed in units of GA half-lives. To emphasize initial formation kinetics, fits were limited to early-time data ($\leq 1\times t_{1/2}$), thereby isolating primary product formation before the onset of significant secondary loss. For kinetics comparison across different experiments, slopes were obtained by taking the derivative of Eq. (3) and evaluating it at $t = 0.5t_{1/2}$:

$$slope = -A * k\ exp(-k * 0.5) \quad (4)$$

The calculated slopes were then normalized following the procedure described in Eq. (2).

The relationships between the observed loss rate of GA (L_{GA}) and the calculated concentration of the triplet-state of DMB ($[^3DMB^*]$) was determined following the approach of Smith et al. (2014). The measured loss rate of GA was expressed as:

$$L_{GA,\ Measured} = k'_{GA,WIN} * [GA]_0 \quad (5)$$

and the theoretical loss rate was calculated as:

$$L_{GA,\ Theoretical} = P_{3DMB*} * f_{GA,DMB} \quad (6)$$

where P_{3DMB*} is the production rate of $^3DMB^*$ and $f_{GA,DMB}$ is the fraction of $^3DMB^*$ reacting with GA (details in Supplementary Section 1).

2.5.2 Water uptake modelling

Water uptake by salts in the SPP were modeled using osmotic coefficients (Φ), which relate molality (m) and water activity (a_i) (Hamer and Yung chi, 1972):

$$\Phi = -\frac{1000}{v*m*M_i}\ln(a_i) \quad (7)$$

where v is the number of ions per electrolyte and M_i is the molar mass of water. Molality-activity relationships were fit to polynomial functions to estimate salt concentrations at specific RH values.

2.5.3 HR-AMS Data Processing and Positive Matrix Factorization (PMF) Analysis

The HR-AMS data were processed using the standard HR-AMS data analysis toolkits (SQUIRREL v1.63H and PIKA v1.23H). Despite the use of a high-capacity silica gel drier, significant particle-phase water signals were observed. To avoid overestimating organic-associated water, Org-H_xO^+ signals were parameterized using the method from Jiang et al. (2021) for GA-aqSOA: Org-H_2O^+ = 0.4×CO_2^+, Org-HO^+ = 0.25×Org-H_2O^+, and Org-O^+ = 0.04×Org-H_2O^+. In addition, the CO^+ signal was also parameterized, using CO^+ = 0.7×CO_2^+, based on phenolic aqSOA spectra from Yu et al. (2016). The internal standard ($^{34}SO_4$) was quantified following the procedures described in Niedek et al. (2023), and SOA yields were calculated as in Jiang et. al (2021). Briefly, a known quantity of $^{34}SO_4$ was added to each aliquot prior to HR-AMS analysis. The $^{34}SO_4$ signal, measured concurrently with the organic aerosol signal in the AMS, serves as an internal reference to quantify the liquid-phase

concentration of organics in the aliquots. The SOA yield was then determined from the increase in the AMS-measured organic signal relative to the corresponding decrease in GA concentration measured by HPLC.

PMF was applied to the high-resolution mass spectra (HRMS) of the organic fraction of the HR-AMS data using the PMF Evaluation Toolkit (v3.08), with input matrices from Experiments 1-13. A four-factor solution was chosen based on the evaluation criteria outlined by Zhang et al (2011). Selecting fewer factors led to high residuals while selecting more factors lead to factor splitting. The four-factor solution also minimized the sum of the weighted squared residuals. Three factors were interpreted as successive generations of GA-derived aqSOA, while the fourth represented background contributions from unreacted GA, consistent with the findings of Jiang et al. (2021). While the same PMF methodology was applied to all experiments, Section 3.2.2 focuses on results from Experiment 7. This experiment exhibited the most extensive GA decay and, consequently, the most pronounced SOA evolution, allowing clear resolution of all three generations of GA-derived aqSOA described in Jiang et al., 2021. In other experiments with less GA decay, only the first and second generations were partially resolved.

3 Results and discussion

3.1 Characterization of the Short Pathlength Photoreactor (SPP)

The SPP enables precise control of RH and T across a wide operating range, enabling experiments that simulate diverse liquid water content (LWC) conditions. As illustrated in Figure 1, the system includes four independent temperature control units: two regulate the reaction chamber (a Peltier device embedded in the chamber base and a circulating water-cooler), while the other two control the temperature of the humidified N_2 stream via heated water and gas lines. Together, these components maintain stable and reproducible RH and T inside the chamber.

Figure a shows a representative long-term record of the chamber T and RH. In this experiment, the system was set to 20 °C and ~60% RH. In practice, the chamber temperature stabilized slightly above the setpoint (22 – 24 °C), likely due to the continuous influx of warm, humid N_2 and minor fluctuations in ambient laboratory temperature that tracked the day-night cycle. For our model system of GA+DMB, this small variation in temperature over hours is unlikely to influence the radical chemistry enough to significantly change the resulting aqSOA chemistry. RH stabilization typically required several hours to equilibrate the water and gas lines, after which RH remained within ±5% of the target value, even after brief chamber openings for sample collection.

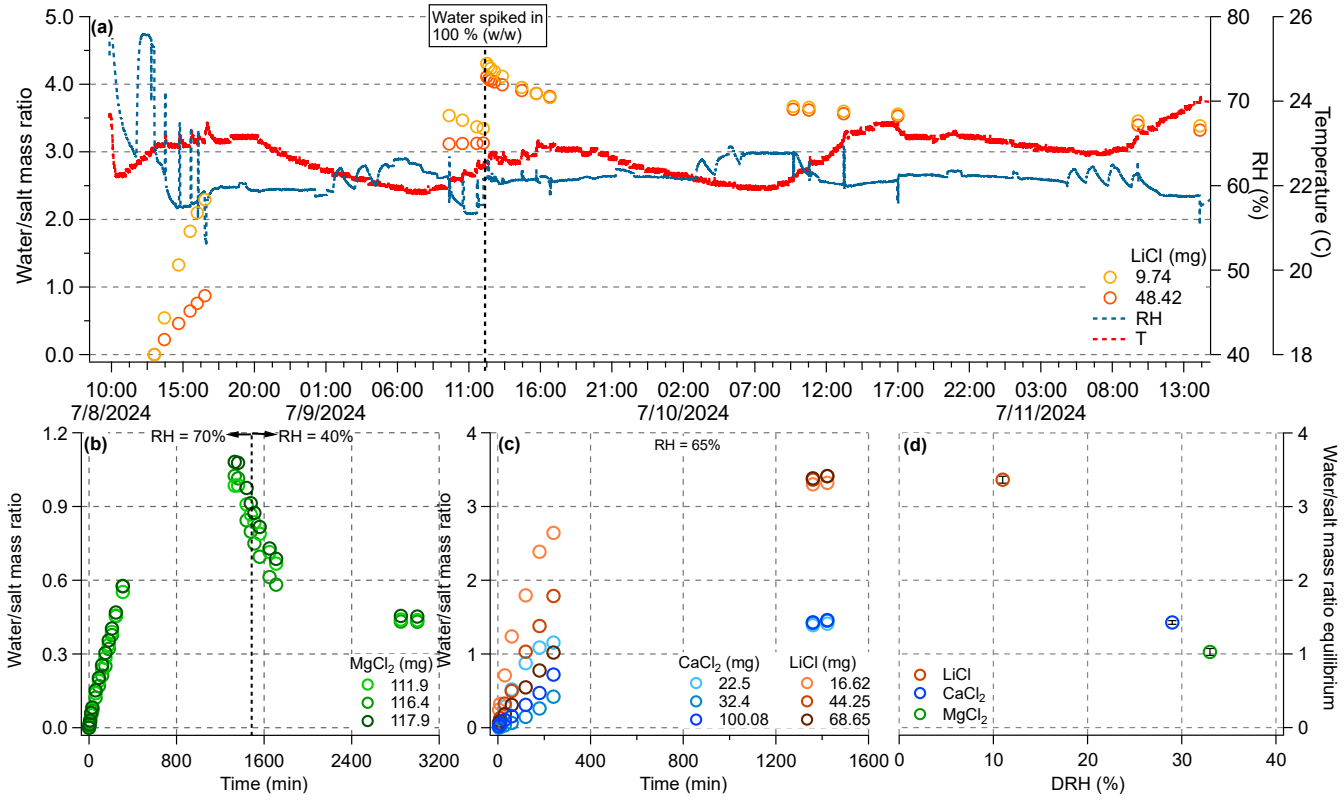

Figure 2: (a) Time series of temperature (T) and relative humidity (RH) inside the SPP reaction chamber, recorded by the Elitech probe, shown alongside water uptake by LiCl samples. (b) Water uptake by $MgCl_2$ at two different RH setpoints. (c) Water uptake by LiCl and $CaCl_2$ under constant RH conditions. (d) Equilibrium water-to-salt mass ratio as a function of the salt deliquescence RH (DRH) for the three salts at their highest RH exposure. All water uptake measurements were performed on salts placed in secondary containers within the SPP reaction chamber.

Because ALW systems often contain high concentrations of light-absorbing species such as nitrate and aromatics, photochemical experiments must account for both optical attenuation and potential photothermal effects. As shown in Figure S1, both GA and DMB absorb significantly within the tropospheric solar spectrum. At [DMB] = 1 mM and an optical pathlength of 0.3 cm, ~ 87 % of incident photons were absorbed; however, the solution temperature increased by only ~1°C above the 20 °C setpoint (Figure S2). This minimal temperature rise, controlled by the internal Peltier cooler and external water bath, demonstrates the SPP's ability to effectively minimize photothermal heating even under highly absorbing conditions.

The SPP also allows for regulation of the liquid water mass in the reaction system via RH control and salt deliquescence. As shown in Figure a-c, equilibrium water uptake by $MgCl_2$, $CaCl_2$, and LiCl was achieved by selecting appropriate RH–salt combinations (see Table S1). For example, $MgCl_2$ exposed to 80% RH absorbed water until reaching equilibrium, which was reversed upon lowering the RH to 40%. The rate of water uptake depended on the initial salt mass, with smaller masses equilibrating faster. As illustrated in Figure d, the equilibrium LWC decreased with increasing deliquescence RH (DRH) and

was largely independent of the total salt mass. The measured water uptake values exhibit moderate agreement with those predicted by the osmotic coefficient-based model (Figure 3). While LiCl displays the largest deviation, the correspondence between predicted and observed values across all salts is generally good under the experimental conditions examined. These results confirmed that the desired solution compositions in the SPP can be reproducibly achieved by choosing suitable combinations of salt type and RH.

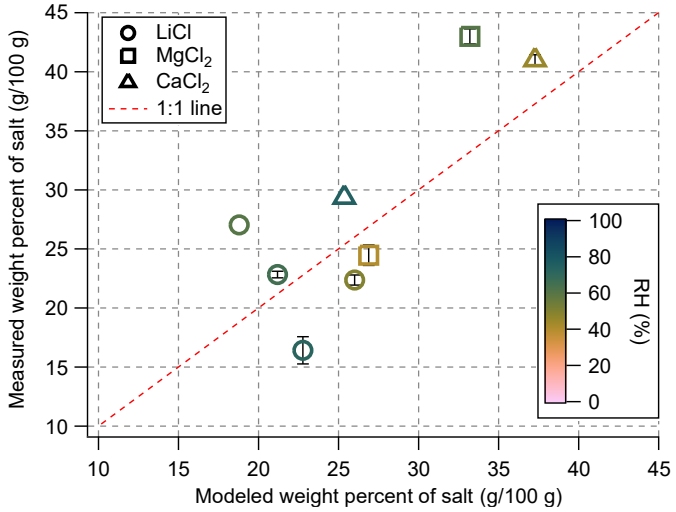

Figure 3: Comparison of measured and predicted values of the weight percent of salt (g-salt/100 g-solution) for LiCl, $MgCl_2$, and $CaCl_2$ across a range of RH conditions. Predicted values were calculated using osmotic coefficient-based water uptake modeling. Data points are averages from replicate experiments and error bars are ± 1 standard deviation.

At high solute concentrations, increased light absorption can limit photon availability within the reaction solution. Under cloud-water conditions, where DMB concentrations are low (e.g., 0.01 mM), only ~ 7 % of incident light at 322 nm is absorbed even with a 1 cm optical pathlength. In contrast, under ALW-like conditions, elevated [DMB] significantly reduces light transmittance, as reflected by lower $j_{2\text{-NB}}$ (Figure 4), consistent with model predictions. While more traditional photoreactors ca be made airtight, modifying ambient conditions inside the reaction chamber can be challenging. Additionally, given the large liquid volumes typically required with standard cuvettes, the ambient conditions, solution composition, and ionic strengths reached here with the SPP represent a significant step forward in laboratory-based explorations of atmospherically relevant condensed-phase chemistry.

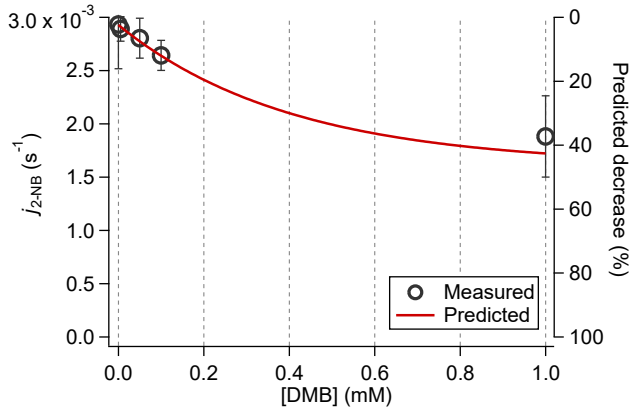

Figure 4: Expected vs. measured decreases in $j_{2\text{-NB}}$ in solutions of DMB with a 0.3 cm pathlength. A description of the model used to predict $j_{2\text{-NB}}$ can be found in the Supplementary Section S1.

To quantify light attenuation, screening factors (S_λ) for solutions containing GA and DMB were calculated across the concentration range in Table 1 using Eq. (1). S_λ represents the fractional photon transmission, where $S_\lambda = 1$ indicates full transmittance and lower values indicate stronger attenuation. Under the most absorbing condition we considered (i.e., [GA] = 2 mM and [DMB] = 0.1 mM) and an SPP pathlength of 0.3 cm, $S_\lambda = 0.74$, indicating moderate absorption. For a conventional 1 cm pathlength, S_λ decreases to 0.14, illustrating the severity of light screening These findings highlight the advantage of the SPP's short pathlength design in minimizing optical attenuation and enabling controlled photochemical experiments under highly absorbing ALW-like conditions.

The SPP's top-down illumination design allows the optical pathlength (and therefore solution absorbance) to be adjusted by varying the solution volume, providing flexibility for optimizing experimental conditions. This represents an advantage over more traditional photoreactors where the pathlength is set by cuvette dimensions and may be difficult to modify, making light screening a significant impediment in solutions with moderate-to-high absorbance. The illumination source can also be easily exchanged to accommodate different applications. In this study, a xenon arc lamp was used to provide a broadband, spatially uniform light field ideal for generating triplet-state species ($^3C^*$). Complementary tests using LED arrays demonstrated that the SPP is equally compatible with narrowband, tunable light sources. To evaluate LED performance, photochemical experiments were conducted using rose bengal as a photosensitizer to generate singlet oxygen ($^1O_2$) under green light irradiation (520 nm) for the oxidation of furfuryl alcohol (FFA), a standard actinometric probe (Arciva et al., 2025). As shown in Figure S3, reactions performed in small secondary vessels positioned beneath different LEDs exhibited up to a 15% variation in FFA decay rates, attributed to differences in individual LED photon flux. This variation is modest and can be corrected by measuring the $j_{2\text{-NB}}$ value for each LED, or, alternatively, by employing a single reaction vessel with vigorous stirring and j_{2NB}-based photon flux calibration. While the remaining sections focus on a model system of GA and DMB photochemistry, the ability to easily swap light sources opens up a broad spectrum of photochemical systems. Overall, these results confirm that the SPP can accommodate both broadband and LED-based illumination while maintaining precise optical and thermal control.

3.2 Photosensitized oxidation of GA under cloud/fog water conditions: validation and comparison to previous work

3.2.1 Bulk SOA comparison

To validate the SPP system, we first replicated photosensitized GA oxidation experiments under cloud/fog water conditions following Jiang et al. (2021) and Ma et al. (2021). Results from these earlier studies, conducted using the RPR-200 and the small tower (ST) photoreactors, are compared with the SPP-based Experiment 1 in Figure a (leftmost three bars). All three experiments used identical initial solution compositions but were performed in different photoreactor configurations: the SPP and ST both used xenon arc lamps but differed in optical pathlength (0.3 cm vs. 2 cm), while the RPR-200 used a set of fluorescent lamps with a distinct spectral output that simulates sunlight illumination (Figure S1).

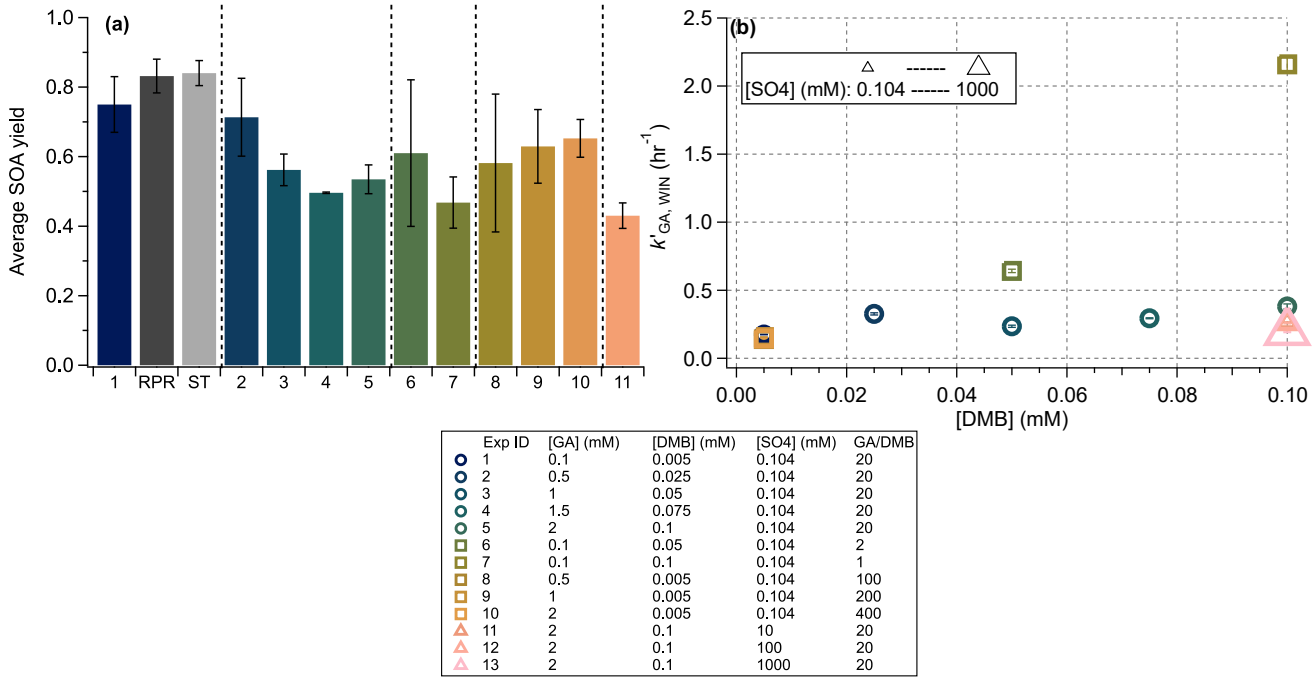

Exp ID	[GA] (mM)	[DMB] (mM)	[SO4] (mM)	GA/DMB
1	0.1	0.005	0.104	20
2	0.5	0.025	0.104	20
3	1	0.05	0.104	20
4	1.5	0.075	0.104	20
5	2	0.1	0.104	20
6	0.1	0.05	0.104	2
7	0.1	0.1	0.104	1
8	0.5	0.005	0.104	100
9	1	0.005	0.104	200
10	2	0.005	0.104	400
11	2	0.1	10	20
12	2	0.1	100	20
13	2	0.1	1000	20

Figure 5: (a) Average SOA yields calculated over the entire illumination period for each experiment. Error bars indicate one standard deviation. Results from the RPR and ST experiments are displayed adjacent to Experiment 1 for comparison. Experiments 12 and 13 are excluded due to high background organic signals at high [SO_4^{2-}], which precluded reliable SOA yield determination. (b) Pseudo-first-order rate constants for GA decay under Davis winter solstice conditions ($k'_{GA,WIN}$) for all experiments. Abbreviated reaction conditions are summarized in the figure legend, with full details provided in Table 1. In (b), maker colors distinguish experimental conditions: circles represent the base experiments where GA and DMB concentrations varied while maintaining a fixed GA/DMB ratio of 20; squares represent experiments where the GA/DMB ratio was modified (by changing either $[GA]_0$ or $[DMB]_0$); triangles represent experiments where [SO_4] was altered while keeping GA/DMB = 20. The size of each triangle scales with [SO_4], allowing visual differentiation of these experiments.

Despite these differences in illumination and reactor geometry, all systems produced highly consistent SOA mass yields for the GA + $^3C^*$ reaction (~80%, Figure). This agreement highlights the robustness of the SPP design and confirms the reproducibility of GA photochemistry across different experimental setups. A more detailed comparison between the SPP and

ST systems is possible due to their shared light source. As shown in Figure S4, the HRMS of aqSOA collected at one GA $t_{1/2}$ are broadly similar between the two reactors. Minor differences are observed at low m/z, where the ST spectrum exhibited relatively enhanced signals of low *m/z* hydrocarbon ions ($C_xH_y^+$), which were absent in both the SPP data and previous RPR-200 experiments (Jiang et al., 2021). This discrepancy likely reflects minor contamination in the ST experiment rather than fundamental chemical differences. Indeed, the two spectra are nearly identical in the high m/z region, dominated by GA dimers and functionalized products (Figure S4). This line of evidence, along with the discussion below in Sections 3.2.2 and 3.3, confirms that phenol-derived aqSOA formed via photosensitized aqueous-phase photochemistry is relatively insensitive to reactor configuration and produces chemically consistent outcomes across systems. The GA + DMB system thus represents a robust and reproducible model for studying aqSOA formation under atmospherically relevant conditions.

3.2.2 Resolving GA+DMB photochemistry via PMF analysis

PMF was applied to characterize the chemical evolution of GA-derived aqSOA, following the approach of Jiang et al (2021). In contrast to that study, which analyzed aqSOA in real time, the present work used discrete sample collection, resulting in lower temporal resolution. PMF was first performed on the combined dataset (Experiments 1-13) and then on individual experiments to assess consistency under different experimental conditions.

In experiments with limited GA decay (< 50%), factor profiles were dominated by oligomerization products, and the first-generation aqSOA factor identified in Jiang et al. (2021) was consistently split across multiple factors, making it difficult to ascertain whether a distinct second-generation factor had been properly resolved. In contrast, experiments with more extensive GA loss (≥ 75%) yielded well-defined profiles, revealing three chemically distinct factors corresponding to successive stages of oxidation and fragmentation.

Experiment 7, which exhibited the greatest extent of GA decay, was analyzed in detail as it represents the most advanced reaction stage and allows direct comparison with Jiang et al. (2021). A summary of the PMF diagnostics for this analysis is shown in Figure S5. As shown in Figure 6a and 6b, the temporal trends of the factors agree well with those reported previously, supporting a consistent interpretation in terms of first-, second-, and third-generation aqSOA formation. The corresponding HRMS factor profiles (Figure 6c-e) further support this interpretation. The first generation aqSOA is marked by oligomerization tracers such as $C_{18}H_{19}O_5^+$. The second-generation factor shows reduced oligomer signal and an increase in mid- to-low m/z ions, indicating progressive functionalization and fragmentation of initial products. The third-generation factor shows the most extensive fragmentation (loss of high m/z ions) and the highest degree of oxidation, characteristic of highly aged aqSOA.

Despite differences in reactor designs, light sources, sampling time resolution, and initial $[GA]_0/[DMB]_0$ ratio, the PMF results from the SPP closely mirrored those of Jiang et al. (2021). This consistency underscores the SPP's capability to produce chemically meaningful and reproducible results that are consistent with established aqSOA formation pathways. Experiment 1 serves as this validation case, while the subsequent experiments extend the framework to more concentrated, atmospherically

relevant conditions—approaching those found in ALW. These additional experiments highlight the SPP's strength in enabling systematic exploration of aqueous-phase chemical kinetics beyond surface-based systems examined previously.

Furthermore, cross-experiment comparisons within the SPP dataset and against Jiang et. al. (2021) study reveal only minor chemical variability, even under substantially varying experimental conditions such as organic concentrations and ionic strength. While the kinetics of GA decay and aqSOA production are affected by organic concentration and ionic strength, the bulk chemical composition of the aqSOA is relatively insensitive to these conditions suggesting that under more ALW-like conditions, the chemical characteristics of phenolic aqSOA may be fairly constant.

Finally, Figure S6 summarizes PMF spectral cross-correlations across representative experiments spanning a wide range of GA and DMB concentrations. Pearson correlation coefficients (r) for the $C_xH_y^+$, $C_xH_yO_1^+$, and $C_xH_yO_{>1}^+$ ion families all exceeded 0.62, with lower values generally attributable to a small number of low-*m/z* ions (<30) that are likely affected by background noise. Overall, these results demonstrate that the aqueous-phase chemical evolution of GA + ^{3}DMB*-derived aqSOA is highly reproducible and broadly insensitive to experimental variability. This chemical robustness supports the use of the GA+DMB system as a reliable model framework for interpreting ambient AMS observations and for elucidating aqSOA formation from biomass-burning emissions under diverse atmospheric conditions.

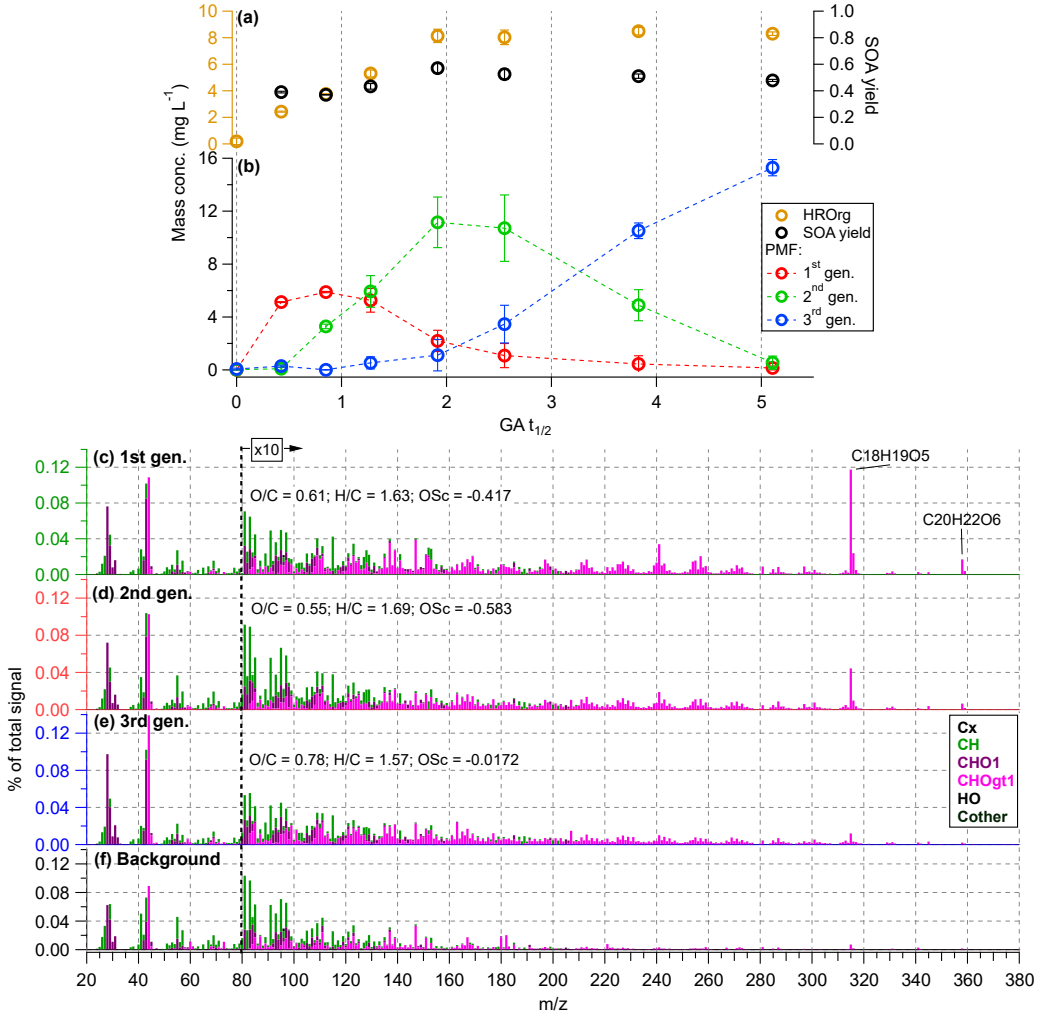

Figure 6: Time series data for Experiment 7 ($[GA]_0$ = 0.1 mM, $[DMB]_0$ = 0.1 mM, $[SO_4^{2-}]_0$ = 0.104 mM), showing (a) evolution of total organic concentration and SOA yield and (b) the four-factor PMF solution, showing the evolution of distinct generations of GA-derived aqSOA. Data points are the averages from multiple samples, with error bars indicating the corresponding standard deviations. The HRMS for the PMF solution are shown in (c-f).

3.3 Photosensitized oxidation of GA under varying aqueous-phase conditions

Figure summarizes SOA yields and GA decay rates from Experiments 1 – 13 conducted using the SPP, covering a range of initial GA concentrations ($[GA]_0$), the ratio of initial concentrations of GA and DMB ($[GA]_0/[DMB]_0$) (reflecting the precursor-to-oxidant balance), and salt concentrations. The normalized pseudo-first-order decay rates of GA under midday winter solstice condition in Davis ($k'_{GA,WIN}$) varied by more than an order of magnitude, with corresponding SOA yields ranging from 0.43 to 0.85.

As shown in Figure b, $k'_{GA,WIN}$ is influenced by both $[DMB]_0$ and $[GA]_0/[DMB]_0$. At fixed $[DMB]_0$ and ionic strength, increasing $[GA]_0$ led to a modest decline in $k'_{GA,WIN}$ (Figure S7a), consistent with previous findings that phenols compete with dissolved oxygen for triplet-state molecules ($^3C^*$), reducing the steady-state $[^3C^*]$ (Ma et al., 2021; Smith et al., 2014). This trend was well described by a kinetic model predicting $k'_{GA,WIN} \propto P_{3DMB^*}/[GA]$ (Figure S7b). In contrast, decreasing $[GA]_0/[DMB]_0$ caused a large increase in $k'_{GA,WIN}$ (Figure b), because of the higher $[^3DMB^*]$. When $[GA]_0/[DMB]_0$ was maintained constant, $k'_{GA,WIN}$ rose slightly with $[GA]_0$, but the absolute GA loss rate increased substantially and agreed well with theoretical expectations (Figure a). This enhancement likely reflects the balance between competing effects: higher $[DMB]_0$ boosts $^3DMB^*$ production, while higher $[GA]_0$ simultaneously increases the sink strength for $^3DMB^*$.

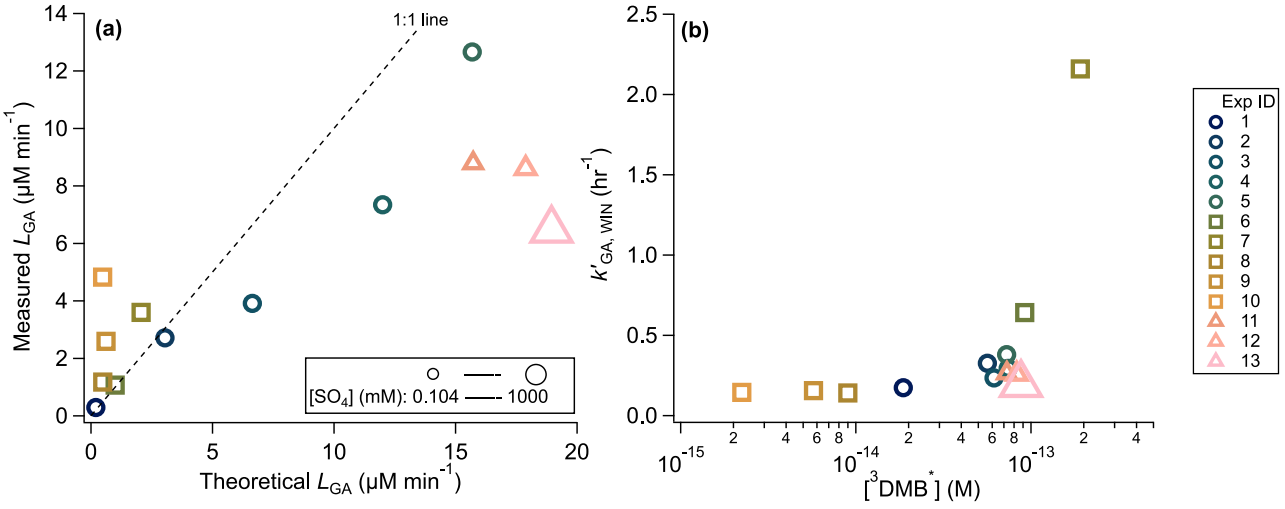

Figure 7: (a) Comparison of the measured vs. theoretical loss rates of GA under various experimental conditions. Marker size reflects the corresponding sulfate concentration, ranging from 0.104 mM to 1000 mM. (b) Pseudo-first order rate constant for GA loss plotted against the calculated steady-state $^3DMB^*$ concentrations. Experimental conditions are color-coded by experiment ID and shape-coded by experimental grouping (see legend). Additional details on the rate constant and $[^3DMB^*]$ calculations can be found in Supplementary Section S1.

Ionic strength also exerted a measurable influence, with $k'_{GA,WIN}$ decreasing by ~ 48% between 0 and 2 M $(NH_4)_2SO_4$ concentrations (Table 1). Although Ma et al. (2021) observed a slight, statistically insignificant increase in $k'_{GA,WIN}$ under 2M $(NH_4)_2SO_4$, direct comparisons between the two studies are limited due to differing $[GA]_0$ and $[DMB]_0$ conditions. The divergence may reflect shifts in the dominant reaction pathways under different solute conditions.

To further evaluate these relationships, measured GA loss rates were compared with theoretical predictions (See Section S1 for calculations). As shown in Figure a, a strong linear correlation was observed, though deviations from 1:1 relationship occurred due to the assumptions in the photon flux scaling and temporal variation in the SPP light field. Experiments 8-10 ($[GA]_0/[DMB]_0 > 20$) showed higher-than-expected loss rates, suggesting that $[GA]_0$ has a stronger effect on decay rate than predicted. In contrast, Experiments 11-13 (high $[SO_4^{2-}]$) displayed lower-than-expected GA loss rates, likely reflecting ionic strength effects on $^3DMB^*$ production or GA-$^3DMB^*$ reaction kinetics. These results are consistent with prior studies showing

salinity-dependent effects on singlet oxygen and triplet-state generation in both natural waters (e.g. (Glover and Rosario-Ortiz, 2013; Mckay et al., 2017; Parker et al., 2013)) and model systems (e.g. (Aggarwal et al., 2007; Appiani et al., 2017; Núñez et al., 2014; Parker et al., 2013)). Although ion-induced changes in excited-state behavior are well-documented, their direction and magnitude are highly system-specific. Nevertheless, dissolved ions are known to modify triplet-state quenching rates (Parker et al., 2013; Treinin et al., 1983), which may in turn influence the photooxidation kinetics of atmospheric species like phenols under different ionic strength regimes.

3.4. Influence of aqueous-phase conditions on aqSOA composition

To investigate the molecular-level impacts of ALW-like conditions on aqSOA chemistry, Figure shows the initial formation rates of two HR-AMS tracer ions – $C_{18}H_{19}O_5^+$ (a marker for GA dimer, representing first-generation aqSOA) and $C_{14}H_{11}O_3^+$ (a marker for second-generation oxidation products) – plotted against either $[GA]_0^2$ (Figure a, c) or ionic strength (Figure b, d). The complete set of formation rates for these ions for all experiments is provided in Table 1 and Figure S8.

Both tracer ions exhibited strong correlations with $[GA]_0^2$, indicating that their formation is primarily governed by a bimolecular oligomerization process. While $C_{14}H_{11}O_3^+$ is generally associated with second-generation oxidation products rather than direct oligomers (Jiang et al., 2023), oligomerization and functionalization likely proceed concurrently. Moreover, since many reactants involved in functionalization are themselves oligomeric species, the observed correlation with $[GA]_0^2$ is consistent with this mechanistic framework.

Formation rates increased linearly with $[GA]_0^2$ but were largely insensitive to $[DMB]_0$ within the range studied (Figure S8). Notably, the rise in dimer formation rates in Experiments 8-10 outpaced that in Experiments 1-5, even though both sets involved in identical increases in $[GA]_0$ and only the later included increases in $[DMB]_0$. Conversely, in Experiments 6-7, where $[DMB]_0$ was increased without changing $[GA]_0$, dimer formation rates remained low, only marginally faster than the base cloud/fog water case (Experiment 1). These results confirm that GA, rather than $^3DMB^*$, is the limiting reagent under most conditions. They further underscore the catalytic nature of $^3C^*$-mediated photochemistry (Smith et al., 2014). Even at relatively low [DMB], phenolic dimer formation appears limited by the availability of phenolic precursors rather than by $[^3DMB^*]$. The weaker response of dimer formation rates to $[DMB]_0$ (as in Experiments 1-5) may be partly attributed to light screening effects at higher DMB concentrations ($S_\lambda = 0.82$ at [DMB] = 0.1 mM), which could reduce the effective photon flux and slow radical generation.

Experiments 11-13, conducted under elevated ionic strength conditions (0.003-3 M), showed 40–100% higher dimer formation rates compared to Experiment 5, which had the same $[GA]_0$ but a much lower ionic strength (0.0003 M). This enhancement indicates that ionic strength significantly influences phenol-$^3C^*$ photochemistry.

While previous studies have reported mixed findings regarding salt effects (a general term meant to encompass ionic strength as well as other salt-related effects described in previous work), most observed only minor effects at molar sulfate concentrations (Loisel et al., 2021; Ma et al., 2021; Zhou et al., 2019). Potential contributing factors include reduced oxygen solubility (Geng and Duan, 2010; Millero et al., 2002) and altered gas-aqueous partitioning (Mekic et al., 2020; Wang et al.,

2021), which can modify phenolic decay rates under saline conditions. However, oxygen availability likely plays a minor role in oligomerization, as the expected decrease in $[O_2]$ is small (see Table S2). For instance, a 35% reduction in $[O_2]$ – from 0.1 mM to 1000 mM ammonium sulfate – corresponded to a twofold increase in oligomerization rate, an effect more plausibly driven by ionic-strength-induced changes in triplet-state or radical chemistry. Overall, these results suggest that salts may modulate phenoxy radical formation or subsequent coupling reactions, both of which are essential steps in phenolic dimerization (Yu et al., 2014).

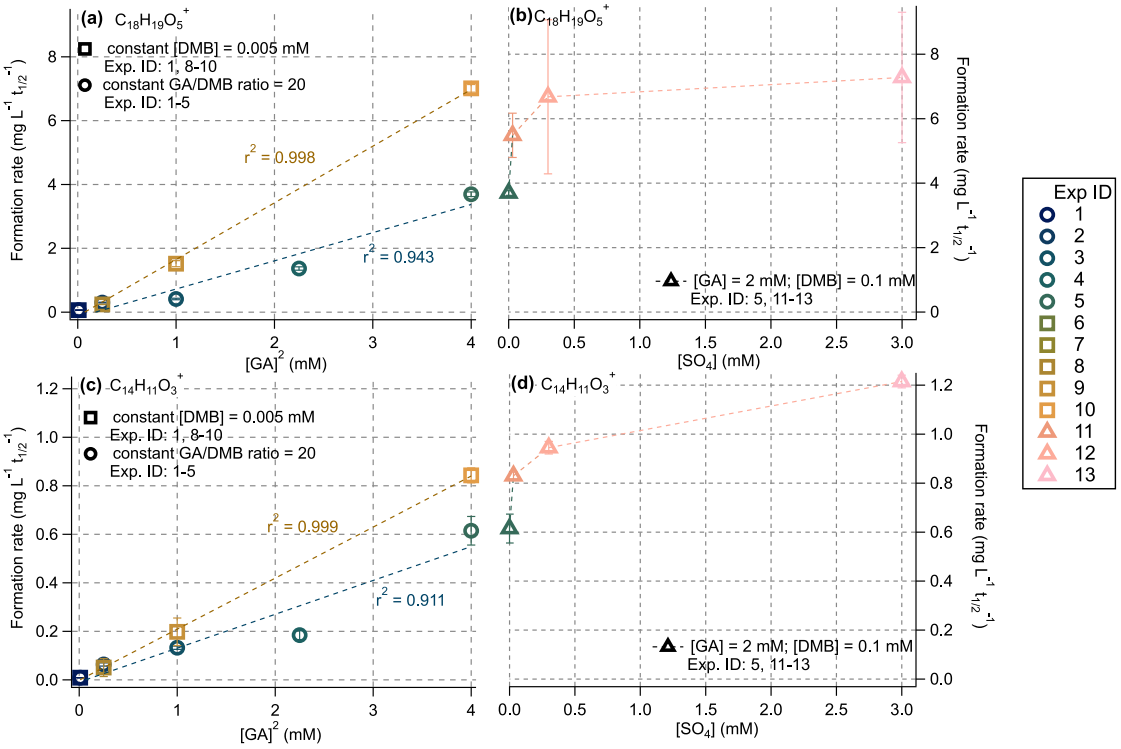

Figure 8: Formation rates of (a, b) $C_{18}H_{19}O_5^+$ (a major GA dimer tracer ion) and (c, d) $C_{14}H_{11}O_3^+$ (a likely second-generation product tracer) plotted against either $[GA]^2$ or ionic strength for several series of experiments (see inset text legend for experiment IDs). Error bars represent propagated uncertainties based on the standard deviations of the fitted coefficients. Reaction conditions are summarized in Table 1 and details regarding the rate-fitting procedures are provided in Section Error! Reference source not found.**. All experimental data were fit using single-exponential functions, except for the $C_{14}H_{11}O_3^+$ in Experiments 11-13, where a linear model was used due to poor exponential fit quality. Time-resolved kinetic data used to obtain the fitted values are shown in Figure S9.**

4 Conclusions

This study demonstrates the capability of a newly developed short-pathlength photoreactor (SPP) for investigating aqueous-phase photochemistry under atmospherically relevant conditions. The SPP integrates a humidity-controlled chamber with interchangeable light sources and reaction vessels, enabling precise control over T, RH, and LWC. Salt deliquescence experiments confirmed that target solution conditions can be reproducibly achieved by choosing appropriate salt-RH

combinations. The short optical pathlength effectively mitigates light attenuation, enabling photochemical experiments under strongly absorbing conditions that are not accessible with conventional photoreactor designs.

Under ALW-like conditions – characterized by elevated concentrations of organic and inorganic solutes – the SPP revealed that while the overall aqSOA composition remained largely similar across reaction conditions, reaction pathways and product distributions varied with solution composition. SOA yields generally decreased with increasing concentrations of GA and DMB, while oligomerization and functionalization were strongly enhanced by higher GA concentrations. In contrast, the photosensitizer DMB concentration had a minimal impact. Ionic strength had only a modest effect on GA photodegradation rates, but more noticeably affected oligomerization and product composition. These findings are particularly relevant to ALW systems, where both organic and inorganic solute concentrations are often significantly higher than those typically found in cloud and fog waters – environments that have dominated laboratory aqSOA studies to date.

More broadly, the SPP, especially when integrated with micro-nebulization aerosol mass spectrometry (MN-AMS; Niedek et al., 2023), provides a robust and versatile platform for mechanistic studies of aqSOA formation and aging. Its ability to accommodate both dilute and concentrated conditions make it well-suited for probing the full continuum of atmospheric aqueous environments, from cloud and fog water to concentrate aerosol liquid water systems.

Data availability

All data sets including HR-AMS mass spectral data and HPLC chromatograms are available upon request from Qi Zhang, dkwzhang@ucdavis.edu.

Supplement

The document contains additional SPP characterization data as well as additional HR-AMS data for the GA+DMB experiments.

Author contributions

QZ and CA designed the photoreactor, and CN led its development. CN and QZ planned the experimental work, which was carried out by CN with contributions from WJ and AZ. CN and QZ performed data analysis. CN, QZ, and CA wrote and revised the manuscript with input from all authors.

Competing interests

The authors declare that they have no conflict of interest.

5 Acknowledgements

This research was supported by the National Science Foundation (Grant AGS-2220307) and the California Agricultural Experiment Station (Projects CA-D-ETX-2102-H and CA-D-LAW-6403-RR). C.N. also acknowledges additional support from the Jastro-Shields Graduate Research Award at UC Davis.

References

Aggarwal, L. P. F., Baptista, M. S., and Borissevitch, I. E.: Effects of NaCl upon TPPS4 triplet state characteristics and singlet oxygen formation, J. Photochem. Photobiol. A Chem., 186, 187–193, https://doi.org/https://doi.org/10.1016/j.jphotochem.2006.08.003, 2007.

Anastasio, C. and McGregor, K. G.: Chemistry of fog waters in California's Central Valley: 1. In situ photoformation of hydroxyl radical and singlet molecular oxygen, Atmos. Environ., 35, 1079–1089, https://doi.org/10.1016/S1352-2310(00)00281-8, 2001.

Appiani, E., Ossola, R., Latch, D. E., Erickson, P. R., and McNeill, K.: Aqueous singlet oxygen reaction kinetics of furfuryl alcohol: effect of temperature, pH, and salt content, Environ. Sci. Process. Impacts, 19, 507–516, https://doi.org/10.1039/C6EM00646A, 2017.

Arciva, S., Niedek, C., Mavis, C., Yoon, M., Sanchez, M. E., Zhang, Q., and Anastasio, C.: Aqueous ·oH Oxidation of Highly Substituted Phenols as a Source of Secondary Organic Aerosol, Environ. Sci. Technol., 56, 9959–9967, https://doi.org/10.1021/acs.est.2c02225, 2022.

Arciva, S., Zhou, Y., Jiang, W., Ross, A., Zhang, Q., and Anastasio, C.: Aqueous Oxidation of Biomass-Burning Furans by Singlet Molecular Oxygen (1O2*), Environ. Sci. Technol., https://doi.org/10.1021/acs.est.4c10778, 2025.

Bianco, A., Passananti, M., Brigante, M., and Mailhot, G.: Photochemistry of the Cloud Aqueous Phase: A Review, https://doi.org/10.3390/molecules25020423, 2020.

Capel, P. D., Leuenberger, C., and Giger, W.: Hydrophobic organic chemicals in urban fog, Atmos. Environ. Part A. Gen. Top., 25, 1335–1346, https://doi.org/https://doi.org/10.1016/0960-1686(91)90244-2, 1991.

Ervens, B.: Modeling the Processing of Aerosol and Trace Gases in Clouds and Fogs, Chem. Rev., 115, 4157–4198, https://doi.org/10.1021/cr5005887, 2015.

Ervens, B., Turpin, B. J., and Weber, R. J.: Secondary organic aerosol formation in cloud droplets and aqueous particles (aqSOA): a review of laboratory, field and model studies, Atmos. Chem. Phys., 11, 11069–11102, https://doi.org/10.5194/acp-11-11069-2011, 2011.

Farley, R., Zhan, S., Collier, S., Jiang, W., Onasch, T., Shilling, J., Kleinman, L., Sedlacek, A., and Zhang, Q.: Chemical Evolution of Biomass Burning Aerosols Across Wildfire Plumes in the Western U.S.: From Near-Source to Regional Scales, ACS ES&T Air, 2025.

Galbavy, E. S., Ram, K., and Anastasio, C.: 2-Nitrobenzaldehyde as a chemical actinometer for solution and ice

photochemistry, J. Photochem. Photobiol. A Chem., 209, 186–192, https://doi.org/10.1016/j.jphotochem.2009.11.013, 2010.

Geng, M. and Duan, Z.: Prediction of oxygen solubility in pure water and brines up to high temperatures and pressures, Geochim. Cosmochim. Acta, 74, 5631–5640, https://doi.org/https://doi.org/10.1016/j.gca.2010.06.034, 2010.

George, K. M., Ruthenburg, T. C., Smith, J., Yu, L., Zhang, Q., Anastasio, C., and Dillner, A. M.: FT-IR quantification of the carbonyl functional group in aqueous-phase secondary organic aerosol from phenols, Atmos. Environ., 100, 230–237, https://doi.org/10.1016/j.atmosenv.2014.11.011, 2015.

Gilardoni, S., Massoli, P., Paglione, M., Giulianelli, L., Carbone, C., Rinaldi, M., Decesari, S., Sandrini, S., Costabile, F., Gobbi, G. P., Pietrogrande, M. C., Visentin, M., Scotto, F., Fuzzi, S., and Facchini, M. C.: Direct observation of aqueous secondary organic aerosol from biomass-burning emissions, Proc. Natl. Acad. Sci., 113, 10013–10018, https://doi.org/10.1073/pnas.1602212113, 2016.

Glover, C. M. and Rosario-Ortiz, F. L.: Impact of Halides on the Photoproduction of Reactive Intermediates from Organic Matter, Environ. Sci. Technol., 47, 13949–13956, https://doi.org/10.1021/es4026886, 2013.

Hamer, W. J. and Yung chi, Y.: Osmotic Coefficients and Mean Activity Coefficients of Uni univalent Electrolytes in Water at 25°C, J. Phys. Chem. Ref. Data, 1, 1047–1100, https://doi.org/10.1063/1.3253108, 1972.

Herrmann, H., Hoffmann, D., Schaefer, T., Bräuer, P., and Tilgner, A.: Tropospheric aqueous-phase free-radical chemistry: Radical sources, spectra, reaction kinetics and prediction tools, ChemPhysChem, 11, 3796–3822, https://doi.org/10.1002/cphc.201000533, 2010.

Herrmann, H., Schaefer, T., Tilgner, A., Styler, S. A., Weller, C., Teich, M., and Otto, T.: Tropospheric Aqueous-Phase Chemistry: Kinetics, Mechanisms, and Its Coupling to a Changing Gas Phase, Chem. Rev., 115, 4259–4334, https://doi.org/10.1021/cr500447k, 2015.

Hodshire, A., Akherati, A., Alvarado, M. J., Brown-Steiner, B., Jathar, S. H., Jimenez, J. L., Kreidenweis, S. M., Lonsdale, C. R., Onasch, T. B., Ortega, A., and Pierce, J. R.: Aging Effects on Biomass Burning Aerosol Mass and Composition: A Critical Review of Field and Laboratory Studies, Environ. Sci. Technol., https://doi.org/10.1021/acs.est.9b02588, 2019.

Huang, D. D., Zhang, Q., Cheung, H. H. Y., Yu, L., Zhou, S., Anastasio, C., Smith, J. D., and Chan, C. K.: Formation and Evolution of aqSOA from Aqueous-Phase Reactions of Phenolic Carbonyls: Comparison between Ammonium Sulfate and Ammonium Nitrate Solutions, Environ. Sci. Technol., 52, 9215–9224, https://doi.org/10.1021/acs.est.8b03441, 2018.

Hullar, T., Bononi, F. C., Chen, Z., Magadia, D., Palmer, O., Tran, T., Rocca, D., Andreussi, O., Donadio, D., and Anastasio, C.: Photodecay of guaiacol is faster in ice, and even more rapid on ice, than in aqueous solution, Environ. Sci. Process. Impacts, 22, 1666–1677, https://doi.org/10.1039/D0EM00242A, 2020.

Jiang, W., Misovich, M. V., Hettiyadura, A. P. S., Laskin, A., McFall, A. S., Anastasio, C., and Zhang, Q.: Photosensitized Reactions of a Phenolic Carbonyl from Wood Combustion in the Aqueous Phase - Chemical Evolution and Light Absorption Properties of AqSOA, Environ. Sci. Technol., 55, 5199–5211, https://doi.org/10.1021/acs.est.0c07581, 2021.

Jiang, W., Niedek, C., Anastasio, C., and Zhang, Q.: Photoaging of phenolic secondary organic aerosol in the aqueous phase: evolution of chemical and optical properties and effects of oxidants, Atmos. Chem. Phys., 23, 7103–7120,

https://doi.org/10.5194/acp-23-7103-2023, 2023.

Jiang, W., Yu, L., Yee, L., Chhabra, P., Seinfeld, J., Anastasio, C., and Zhang, Q.: Chemical Differences between Phenolic Secondary Organic Aerosol Formed through Gas-Phase and Aqueous-Phase Reactions, ACS Earth Sp. Chem., 8, 2270–2283, https://doi.org/10.1021/acsearthspacechem.4c00204, 2024.

Jimenez, J. L., Canagaratna, M. R., Donahue, N. M., Prevot, A. S. H., Zhang, Q., Kroll, J. H., DeCarlo, P. F., Allan, J. D., Coe, H., Ng, N. L., Aiken, A. C., Docherty, K. S., Ulbrich, I. M., Grieshop, A. P., Robinson, A. L., Duplissy, J., Smith, J. D., Wilson, K. R., Lanz, V. A., Hueglin, C., Sun, Y. L., Tian, J., Laaksonen, A., Raatikainen, T., Rautiainen, J., Vaattovaara, P., Ehn, M., Kulmala, M., Tomlinson, J. M., Collins, D. R., Cubison, M. J., Dunlea, E. J., Huffman, J. A., Onasch, T. B., Alfarra, M. R., Williams, P. I., Bower, K., Kondo, Y., Schneider, J., Drewnick, F., Borrmann, S., Weimer, S., Demerjian, K., Salcedo, D., Cottrell, L., Griffin, R., Takami, A., Miyoshi, T., Hatakeyama, S., Shimono, A., Sun, J. Y., Zhang, Y. M., Dzepina, K., Kimmel, J. R., Sueper, D., Jayne, J. T., Herndon, S. C., Trimborn, A. M., Williams, L. R., Wood, E. C., Middlebrook, A. M., Kolb, C. E., Baltensperger, U., and Worsnop, D. R.: Evolution of organic aerosols in the atmosphere, Science (80-.)., 326, 1525–1529, https://doi.org/10.1126/science.1180353, 2009.

Li, F., Zhou, S., Du, L., Zhao, J., Hang, J., and Wang, X.: Aqueous-phase chemistry of atmospheric phenolic compounds: A critical review of laboratory studies, Sci. Total Environ., 856, 158895, https://doi.org/https://doi.org/10.1016/j.scitotenv.2022.158895, 2023.

Loisel, G., Mekic, M., Liu, S., Song, W., Jiang, B., Wang, Y., Deng, H., and Gligorovski, S.: Ionic strength effect on the formation of organonitrate compounds through photochemical degradation of vanillin in liquid water of aerosols, Atmos. Environ., 246, https://doi.org/10.1016/j.atmosenv.2020.118140, 2021.

Ma, L., Guzman, C., Niedek, C., Tran, T., Zhang, Q., and Anastasio, C.: Kinetics and Mass Yields of Aqueous Secondary Organic Aerosol from Highly Substituted Phenols Reacting with a Triplet Excited State, Environ. Sci. Technol., 55, 5772–5781, https://doi.org/10.1021/acs.est.1c00575, 2021.

McFall, A. S., Johnson, A. W., and Anastasio, C.: Air-Water Partitioning of Biomass Burning Phenols and the Effects of Temperature and Salinity, Environ. Sci. Technol., https://doi.org/10.1021/acs.est.9b06443, 2020.

Mckay, G., Huang, W., Romera-Castillo, C., Crouch, J. E., Rosario-Ortiz, F. L., and Jaffé, R.: Predicting Reactive Intermediate Quantum Yields from Dissolved Organic Matter Photolysis Using Optical Properties and Antioxidant Capacity, Environ. Sci. Technol., 51, 5404–5413, https://doi.org/10.1021/acs.est.6b06372, 2017.

McNeill, V. F.: Aqueous Organic Chemistry in the Atmosphere: Sources and Chemical Processing of Organic Aerosols, Environ. Sci. Technol., 49, 1237–1244, https://doi.org/10.1021/es5043707, 2015.

Mekic, M. and Gligorovski, S.: Ionic strength effects on heterogeneous and multiphase chemistry: Clouds versus aerosol particles, Atmos. Environ., 244, 117911, https://doi.org/https://doi.org/10.1016/j.atmosenv.2020.117911, 2021.

Mekic, M., Wang, Y., Loisel, G., Vione, D., and Gligorovski, S.: Ionic Strength Effect Alters the Heterogeneous Ozone Oxidation of Methoxyphenols in Going from Cloud Droplets to Aerosol Deliquescent Particles, Environ. Sci. Technol., 54, 12898–12907, https://doi.org/10.1021/acs.est.0c03648, 2020.

Millero, F. J., Huang, F., and Laferiere, A. L.: The solubility of oxygen in the major sea salts and their mixtures at 25°C, Geochim. Cosmochim. Acta, 66, 2349–2359, https://doi.org/https://doi.org/10.1016/S0016-7037(02)00838-4, 2002.

Niedek, C. R., Mei, F., Zawadowicz, M. A., Zhu, Z., Schmid, B., and Zhang, Q.: Quantitative chemical assay of nanogram-level particulate matter using aerosol mass spectrometry: characterization of particles collected from uncrewed atmospheric measurement platforms, Atmos. Meas. Tech., 16, 955–968, https://doi.org/10.5194/amt-16-955-2023, 2023.

Núñez, S. C., Garcez, A. S., Kato, I. T., Yoshimura, T. M., Gomes, L., Baptista, M. S., and Ribeiro, M. S.: Effects of ionic strength on the antimicrobial photodynamic efficiency of methylene blue, Photochem. Photobiol. Sci., 13, 595–602, https://doi.org/10.1039/C3PP50325A, 2014.

Pang, H., Zhang, Q., Lu, X., Li, K., Chen, H., Chen, J., Yang, X., Ma, Y., Ma, J., and Huang, C.: Nitrite-Mediated Photooxidation of Vanillin in the Atmospheric Aqueous Phase, Environ. Sci. Technol., 53, 14253–14263, https://doi.org/10.1021/acs.est.9b03649, 2019.

Parker, K. M., Pignatello, J. J., and Mitch, W. A.: Influence of Ionic Strength on Triplet-State Natural Organic Matter Loss by Energy Transfer and Electron Transfer Pathways, Environ. Sci. Technol., 47, 10987–10994, https://doi.org/10.1021/es401900j, 2013.

Parworth, C. L., Young, D. E., Kim, H., Zhang, X., Cappa, C. D., Collier, S., and Zhang, Q.: Wintertime water-soluble aerosol composition and particle water content in Fresno, California, J. Geophys. Res. Atmos., 122, 3155–3170, https://doi.org/https://doi.org/10.1002/2016JD026173, 2017.

Romanias, M. N., Coggon, M. M., Al Ali, F., Burkholder, J. B., Dagaut, P., Decker, Z., Warneke, C., Stockwell, C. E., Roberts, J. M., Tomas, A., Houzel, N., Coeur, C., and Brown, S. S.: Emissions and Atmospheric Chemistry of Furanoids from Biomass Burning: Insights from Laboratory to Atmospheric Observations, ACS Earth Sp. Chem., 8, 857–899, https://doi.org/10.1021/acsearthspacechem.3c00226, 2024.

Sagebiel, J. C. and Seiber, J. N.: Studies on the occurrence and distribution of wood smoke marker compounds in foggy atmospheres, Environ. Toxicol. Chem., 12, 813–822, https://doi.org/10.1002/etc.5620120504, 1993.

Schauer, J. J., Kleeman, M. J., Cass, G. R., and Simoneit, B. R. T.: Measurement of Emissions from Air Pollution Sources. 3. C1−C29 Organic Compounds from Fireplace Combustion of Wood, Environ. Sci. Technol., 35, 1716–1728, https://doi.org/10.1021/es001331e, 2001.

Von Schneidemesser, E., Monks, P. S., Allan, J. D., Bruhwiler, L., Forster, P., Fowler, D., Lauer, A., Morgan, W. T., Paasonen, P., Righi, M., Sindelarova, K., and Sutton, M. A.: Chemistry and the Linkages between Air Quality and Climate Change, Chem. Rev., 115, 3856–3897, https://doi.org/10.1021/acs.chemrev.5b00089, 2015.

Shrivastava, M., Cappa, C. D., Fan, J., Goldstein, A. H., Guenther, A. B., Jimenez, J. L., Kuang, C., Laskin, A., Martin, S. T., Ng, N. L., Petaja, T., Pierce, J. R., Rasch, P. J., Roldin, P., Seinfeld, J. H., Shilling, J., Smith, J. N., Thornton, J. A., Volkamer, R., Wang, J., Worsnop, D. R., Zaveri, R. A., Zelenyuk, A., and Zhang, Q.: Recent advances in understanding secondary organic aerosol: Implications for global climate forcing, Rev. Geophys., 55, 509–559, https://doi.org/https://doi.org/10.1002/2016RG000540, 2017.

Smith, J. D., Sio, V., Yu, L., Zhang, Q., and Anastasio, C.: Secondary organic aerosol production from aqueous reactions of atmospheric phenols with an organic triplet excited state, Environ. Sci. Technol., 48, 1049–1057, https://doi.org/10.1021/es4045715, 2014.

Smith, J. D., Kinney, H., and Anastasio, C.: Aqueous benzene-diols react with an organic triplet excited state and hydroxyl radical to form secondary organic aerosol, Phys. Chem. Chem. Phys., 17, 10227–10237, https://doi.org/10.1039/c4cp06095d, 2015.

Smith, J. D., Kinney, H., and Anastasio, C.: Phenolic carbonyls undergo rapid aqueous photodegradation to form low-volatility, light-absorbing products, Atmos. Environ., 126, 36–44, https://doi.org/https://doi.org/10.1016/j.atmosenv.2015.11.035, 2016.

Sun, Y. L., Zhang, Q., Anastasio, C., and Sun, J.: Insights into secondary organic aerosol formed via aqueous-phase reactions of phenolic compounds based on high resolution mass spectrometry, Atmos. Chem. Phys., 10, 4809–4822, https://doi.org/10.5194/acp-10-4809-2010, 2010.

Tilgner, A., Schaefer, T., Alexander, B., Barth, M., Collett Jr., J. L., Fahey, K. M., Nenes, A., Pye, H. O. T., Herrmann, H., and McNeill, V. F.: Acidity and the multiphase chemistry of atmospheric aqueous particles and clouds, Atmos. Chem. Phys., 21, 13483–13536, https://doi.org/10.5194/acp-21-13483-2021, 2021.

Treinin, A., Loeff, I., Hurley, J. K., and Linschitz, H.: Charge-transfer interactions of excited molecules with inorganic anions: the role of spin-orbit coupling in controlling net electron transfer, Chem. Phys. Lett., 95, 333–338, https://doi.org/https://doi.org/10.1016/0009-2614(83)80569-7, 1983.

Wang, Y., Mekic, M., Li, P., Deng, H., Liu, S., Jiang, B., Jin, B., Vione, D., and Gligorovski, S.: Ionic Strength Effect Triggers Brown Carbon Formation through Heterogeneous Ozone Processing of Ortho-Vanillin, Environ. Sci. Technol., 55, 4553–4564, https://doi.org/10.1021/acs.est.1c00874, 2021.

Yu, L., Smith, J., Laskin, A., Anastasio, C., Laskin, J., and Zhang, Q.: Chemical characterization of SOA formed from aqueous-phase reactions of phenols with the triplet excited state of carbonyl and hydroxyl radical, Atmos. Chem. Phys., 14, 13801–13816, https://doi.org/10.5194/acp-14-13801-2014, 2014.

Yu, L., Smith, J., Laskin, A., M George, K., Anastasio, C., Laskin, J., M Dillner, A., and Zhang, Q.: Molecular transformations of phenolic SOA during photochemical aging in the aqueous phase: Competition among oligomerization, functionalization, and fragmentation, Atmos. Chem. Phys., 16, 4511–4527, https://doi.org/10.5194/acp-16-4511-2016, 2016.

Zhang, G., Peng, X., Sun, W., Fu, Y., Yang, Y., Liu, D., Shi, Z., Tang, M., Wang, X., and Bi, X.: Fog/cloud processing of atmospheric aerosols from a single particle perspective: A review of field observations, Atmos. Environ., 329, 120536, https://doi.org/https://doi.org/10.1016/j.atmosenv.2024.120536, 2024a.

Zhang, J., Shrivastava, M., Ma, L., Jiang, W., Anastasio, C., Zhang, Q., and Zelenyuk, A.: Modeling Novel Aqueous Particle and Cloud Chemistry Processes of Biomass Burning Phenols and Their Potential to Form Secondary Organic Aerosols, Environ. Sci. Technol., 58, 3776–3786, https://doi.org/10.1021/acs.est.3c07762, 2024b.

Zhang, Q., Jimenez, J. L., Canagaratna, M. R., Ulbrich, I. M., Ng, N. L., Worsnop, D. R., and Sun, Y.: Understanding atmospheric organic aerosols via factor analysis of aerosol mass spectrometry: A review, Anal. Bioanal. Chem., 401, 3045–

3067, https://doi.org/10.1007/s00216-011-5355-y, 2011.

Zhou, W., Mekic, M., Liu, J., Loisel, G., Jin, B., Vione, D., and Gligorovski, S.: Ionic strength effects on the photochemical degradation of acetosyringone in atmospheric deliquescent aerosol particles, Atmos. Environ., 198, 83–88, https://doi.org/10.1016/j.atmosenv.2018.10.047, 2019.

620